Charge Polarization at Catalytic Metal-Support Junctions

Part B: Theoretical Modeling of Kelvin Probe Force Microscopy

Tobias Kittel[1†] *and Emil Roduner*[1,2]*

[1] Institute of Physical Chemistry, University of Stuttgart,

Pfaffenwaldring 55, D-70569 Stuttgart, Germany

[2] Department of Chemistry, University of Pretoria, Pretoria 0002, Republic of South Africa

ABSTRACT

Existing models for the analysis of Kelvin probe microscopy experiments are extended and used to analyze the experimental electrical potential profiles for a Pt/TiO_2 model nanoparticle. The derived model reproduces in detail the Kelvin probe image that reveals a characteristic ring-shaped negative charge zone at the surface around the particle: A planar negative charge zone at the surface of the support extends beyond the diameter of the Pt particle. It is compensated mostly by a planar layer of positive charges in the metal across the interface, and by a smaller number of positive charges at the metal-air interface. These latter charges determine the positive electrical potential of the metal particle, and they are likely responsible for the extent of the metal-support interaction in catalytic reactions.

KEYWORDS**:** Noble metal catalysis; metal oxide support; catalyst-support effect; charge polarization; Kelvin probe microscopy

INTRODUCTION

Heterogeneous catalysts are in most cases solids with a large specific surface area with active sites which interact with a substrate that is exposed to these centers from the gas or

liquid phase. The active sites may be of various nature, *e.g.* Brønsted or Lewis acid sites, metal ions embedded in complexes or in the catalyst surface, but very commonly the catalysts are nanosize noble metal particles supported on metal oxides. In these cases it is often the metal particle which exerts the catalytic function, but it can also be the support which is active. In particular, metal oxides are catalytically active for the oxidation of hydrocarbons in Mars-van-Krevelen type reactions. The key step is the reduction of the metal oxide, which depends on the equilibrium between oxygen surface species and oxygen vacancies in the metal oxide. This equilibrium can be influenced by the presence of more or less strongly electron accepting property of supported metal particles. Oxygen anions have to leave behind their excess electrons when they recombine and leave the surface as molecular oxygen. The mechanism is supported by the presence of any electron accepting centers, as has been demonstrated by Acerbi *et al*. who showed that the reduction temperature of cerium oxide decreases depending on the work function of a supported noble metal.[1]

In semiconductor physics, a metal in contact with a semiconducting metal oxide is called a Schottky contact. It is well known that such a configuration leads to a polarization at the metal-support interface by transfer of electrons from the metal particle to the support or *vice versa*, depending on the energetic position of the Fermi level of the metal particle relative to that of donor or acceptor defects in the support. The importance of the effects of a Schottky junction in catalysis was postulated by Frost [2] and even much earlier by Solymosi.[3] A theoretical discussion was given by Ioannidis [4,5] and by Zhdanov and Hagglund,[6,7] with a debate about the applicability of Schottky's model for extended interfaces to nanometer sized particles. Experimental verification of the polarization effect under catalytically relevant conditions has so far been given as infrared spectroscopic observation of shifts of the vibrational frequency of Pt-adsorbed C=O,[9] the modified activity in hydrogenation reactions of aromatics [10,11] or also by macroscopic conductivity measurements of the doped TiO_2

support.[12] These methods are not sufficiently quantitative, and in particular they do not provide the necessary spatial resolution to discriminate between various charge distribution models.

A bulk intrinsic semiconductor like silicon shows a quite miserable electronic conductivity since relatively few electrons are excited across the band gap of on the order of 1 eV from the fully occupied valence band to the empty conduction band. This changes dramatically when a small fraction of atoms (typically one out of $10^4 – 10^7$ atoms) is replaced by donor or acceptor atoms. Si has four valence atoms and makes four bonds. Atoms with five valence electrons like phosphorous are donors. The extra electron occupies an isolated state slightly below the lower edge of the conduction band, so it can be thermally excited into the conduction band, which causes electronic conductivity. Since the charges which carry conductivity are negative (electrons) this type semiconductor is called *n*-type. Alternatively, doping can be by an element with only three valence electrons, like aluminum. Such an atom needs to accept an additional electron to be able to make four bonds. The acceptor state is slightly above the upper band edge of the valence band, and an electron from the valence band can be excited thermally into this vacancy. This then leaves a positive hole in the valence band which leads to *p*-type conductivity.

TiO_2 is a metal oxide with a band gap of 3.2 eV. If it is fully stoichiometric it is a relatively good insulator. In reality, many metal oxides are not exactly stoichiometric. At sufficiently high temperature they may lose two oxygen atoms in the form of O_2, which leaves behind two oxygen vacancies ($V_O^{\bullet\bullet}$) and the four extra electrons of the two former oxygen dianions ($O_O^{\times}$):

$$4\,M_M^{\times} + 2\,O_O^{\times} \xrightarrow{-O_2} 4\,M_M' + 2\,V_O^{\bullet\bullet} \qquad (1)$$

The extra electrons reduce the charge of the original cations ($M_M^{\times}$) by one charge, leaving it one-fold negative relative to the atom in the intact lattice (M_M') as written in the Kröger-Vink convention. Specifically, for TiO_2, the formal Ti(IV) cations become Ti(III) which can be

observed experimentally by EPR.[13] These M'_M centers can act as electron donors to the conduction band

$$M'_M \xrightarrow{-e^-} M^{\times}_M \qquad (2)$$

so that the oxygen deficient TiO_2 behaves as an *n*-type semiconductor, which is the normal state of titania under reducing conditions.[14] Alternatively, the hydroxylated surface of wet titania or surface adsorbed dioxygen can act as acceptor states which trap (excited) electrons from the conduction band, leaving holes in bulk titania and converting it to a *p*-type semiconductor.[15]

So far, this description related to the plain support material. A noble metal particle in contact with this support complicates the situation by modification of the charge carrier concentrations. Acerbi *et al*. reported a correlation between the work function of the supported metal particle and the onset temperature of a test reaction.[1] A nobler element has a higher work function which corresponds to a higher ability to accept electrons from the ceria oxide support, and this promotes the release of neutral oxygen from the bulk of the oxide so that it can react with the gas phase substrate at a lower temperature. The observed effect was taken as clear evidence of the presence of a charge polarization across the interface between metal particle and oxide support. Such an interface between metal and semiconductor is called a Schottky contact. In the reaction reported by Acerbi [1] the metal acts as a promotor and the metal oxide is the active catalyst. More commonly and also in the present work the functions are reversed: the metal oxide is the support and the catalyst is the metal particle. The case is illustrated schematically in Figure 1.

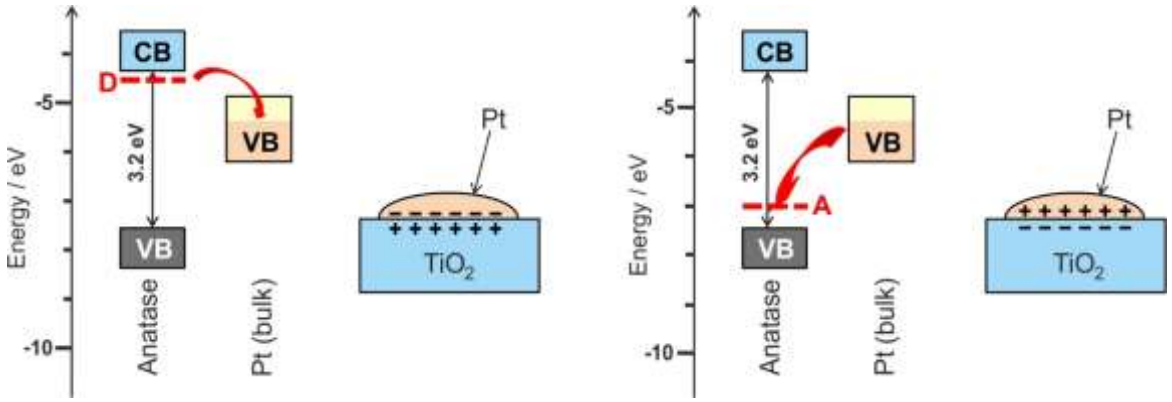

Figure 1. *n*-Type semiconducting anatase with donor states *D* below the lower band edge of the TiO_2 conduction band *CB* but above the Fermi level of bulk Pt, resulting in electron transfer from the support to the metal (left part of Figure), and *p*-type case with acceptor states *A* above the upper edge of the TiO_2 valence band, leading to electron transfer to the support and opposite polarity at the interface (right part of Figure). Reprinted with permission from Ref. 16.

The Fermi level of bulk metallic platinum is within the band gap of anatase (for quantitative values see Figure S3 of companion paper). In this situation the electrons of donor levels below the lower band edge of the conduction band (*n*-type doping, left of Figure 1, Ti(III) in the case of TiO_2) are transferred to Pt, while empty acceptor states above the valence band of the support (*p*-type doping, right of Figure 1, *e.g.* adsorbed O_2 or hydroxylated surface states) are replenished from the metal. In both cases, the compensating opposite charges of the localized defect states in the support remain unaffected, but the electrical conductivity of the oxide support is quenched near the interface where the process leads to a planar capacitor-like double layer of charges. In the following we nevertheless keep the nomenclature of *p*- and *n*-type semiconductors where the transfer of negative charge from the metal occurs to a *p*-type semiconductor support, and *vice versa* for the *n*-type support. Charge redistribution and concomitant shift of the Fermi level by −11 mV has also been reported for UV-irradiated TiO_2 and gold nanoparticles.[17]

The support provides of course a large reservoir of states which can interact with the metal nanoparticle. Across the interface, there is an attractive interaction that drives the transfer, but there is a competing repulsive interaction on each side of the interface that increases with charge density. It is important to note that the attractive interaction between the hole in the metal and the excess electron in the support (Ti(III)) at a distance of 200 pm (Table 1 of Ref. 18) is stabilized by Coulombic attraction of 2.5 eV so that the dimer defect lies below the level of the isolated donor state D in Figure 1. The capacity of defects directly at the interface is limited, but additional charges could be accommodated in the neighborhood. The question is therefore to which extent this charge transfer between metal and support proceeds and what the details of the final charge distribution are. We are not aware of any previous work in this direction, except for a scanning thermoelectric microscopy determination of the local carrier concentration across a semiconductor quantum dot,[19] and it is the aim of the present work to advance the information about the charge distribution and its influence on catalysis.

Kelvin probe force microscopy (KPFM) is a powerful tool [20] and has been used under ultra-high vacuum (UHV) conditions to study with high resolution vacuum deposited platinum particles supported on TiO_2 single crystal surfaces by Sasahara *et al*. and Hiehata *et al*. [21-23] Our intention is to overcome the pressure gap between UHV and catalytically relevant reactions conditions and quantify the metal-support interaction in ambient atmosphere and at ambient temperature with the aim to distinguish between the different descriptions. In this study we first present the theoretical foundations for different models which are in a second part [18] used for the analysis and discussion of experimental data.

A companion paper reports Kelvin probe force microscopy (KPFM) measurements of Pt, Pd and Rh nanoparticles supported on TiO_2, CrO_2 and Al_2O_3 oxides under nitrogen/oxygen atmosphere at ambient pressure.[18] In the KPFM measurement the conductive tip of the atomic force microscope (AFM) is scanned across the sample in constant height above the surface,

i.e. in non-contact mode. The experiment measures the electrical potential due to polarization of the sample by charge transfer across the metal-semiconductor (or insulator) interface. The charge distribution above/below the interface constitutes a dipole which induces a charge in the AFM tip so that we effectively have a capacitor formed by the interface and the tip. The measurements provide clear evidence of the direction and qualitative extent of charge polarization. Here we aim at a quantitative interpretation based on various models for the charge distribution on both sides of the interface and on the surface around the metal particle where experiments have shown a negative rim for some of the samples (see Figure 3 of companion paper).[18] The models assume that the AFM tip is a point probe of a charge distribution for a given shape of the metal particle (see companion paper for a discussion of this assumption).[18] Thus, for each measured point the potential is obtained by integration over the entire charge distribution. The method developed here is used for the analysis of a large number of metal oxide supported Pt, Pd and Rh particles as described in the companion paper.[18] The full details are available in a PhD thesis which can be accessed online.[24]

DISCUSSION

The Model of Sasahara *et al.*[23] for the quantification of the Kelvin signal

The most basic model that has been applied in literature to explain the size of the KPFM signal assumes a symmetric charge distribution about the interface as in a capacitor that consists of two parallel circular plates. Charges of $\pm q$ are separated by a constant distance d given by the sum of the radii of the metal oxide cation and the noble metal atom and form a layer of dipoles. The charges are evenly distributed within a circular area, represented by a charge a density ρ. Their electrostatic response φ that is probed by the point-like AFM tip, positioned above the center of the circle, is given according to Sasahara *et al.*[23] by

$$\varphi = \frac{1}{4\pi\varepsilon_0}\int_0^R \left(\frac{2\pi r\,\rho q}{\sqrt{r^2+h^2}} - \frac{2\pi r\,\rho q}{\sqrt{r^2+(h+d)^2}}\right) \mathrm{d}r = \frac{\rho q}{2\varepsilon_0}\left(\sqrt{R^2+h^2} - \sqrt{R^2+(h+d)^2}\right) \qquad (1)$$

The height h is the sum of the particle height at the center and the scan height above the surface during the Kelvin scan. Deviations of the permeability from the vacuum value ε_0 are neglected in Sasahara's treatment.

It is straightforward to extend Sasahara's one-point model to a trace model in dependence of the tip position. The model is extended to include additional charges located at the particle surface.

Sasahara's model is based on the simple correlation between the electrostatic potential at point $\vec{p}$ which is generated by a point charge q located at the position $\vec{r}$

$$\varphi(\vec{p}) = \frac{1}{4\pi\varepsilon_0}\frac{q}{|\overrightarrow{pr}|} \tag{2}$$

The potential at $\vec{p}$ originating in a multitude of point charges q can be written as the sum of the individual contributions and transformed to the integral over the corresponding space coordinates in dependence of the charge density ρ

$$\varphi(\vec{p}) = \frac{1}{4\pi\varepsilon_0}\sum_i \frac{q}{|\overrightarrow{pr_i}|} \;\Rightarrow\; \frac{1}{4\pi\varepsilon_0}\int \frac{\rho q}{|\overrightarrow{pr}|}\,d\tau \tag{3}$$

Setting the position of the tip as $\vec{p} = (x, 0, z)$ allows us to calculate the potential signal along one axis through the particle center in dependence of the horizontal position x and the vertical tip position z is calculated as the sum of the actual particle height H at a given position and the scan height h_{tip}.

The potential signal of a circular charge distribution at the interface in dependence of the tip position in polar coordinates results to

$$\varphi(x,z) = \frac{1}{4\pi\varepsilon_0}\cdot\frac{\rho q}{\pi R^2}\int_{r=0}^{R}\int_{\phi=0}^{2\pi}\frac{r}{\sqrt{x^2+r^2-2xr\cos\phi+(z-d)^2}} - \frac{r}{\sqrt{x^2+r^2-2xr\cos\phi+(z+d)^2}}\,\mathrm{d}\phi\mathrm{d}r \tag{4}$$

where the parameters are the same as in (1).

The charge density ρ is now determined by equation (4) and the experimental Kelvin signal φ_{Kelvin} at a single tip position $(0, z_{tip})$ above the particle center

$$\varphi(0, z_{\text{tip}}) = \varphi_{\text{tip}} = -\varphi_{\text{Kelvin}} \tag{5}$$

Equation (4) and ρ calculated from equation (5) allow the simulation of the resulting Kelvin signal in dependence of the coordinates (x, z).

For the quantitative analysis we chose non-agglomerated particles with a near-circular interface since it is convenient to use a particle model whose shape can be described analytically in modified cylindrical coordinates. Three different approximations were chosen to develop and test out the method: the oblate spheroid, the cone and the rotational paraboloid, here in the following simply called ellipsoid, cone and paraboloid. They are shown in the upper part of Figure 2 for a typical experimentally observed particle. The particle volume is overestimated by the ellipsoid and underestimated by the cone. The paraboloid agrees best with the actual particle shape, especially at the particle apex, and the full evaluation of all particles [18] was based on the paraboloid only. Models of rotational symmetry also have the advantage that it is sufficient to calculate a one-dimensional trace in any direction across the particle. Normally, this will be directly part of an experimental scan across the center of the particle.

This experimentally observed particle was chosen as a model particle for all following calculations. The lower part of Figure 2 displays the best simulation based on Sasahara's model of a parallel plate conventional capacitor model. While the chosen particle shape has relatively little impact it is obvious that the overall agreement of simulation and experiment is not satisfactory. In particular, the positive rim around the particle, pointed out in Figure 4 of the companion paper,[18] which corresponds to negative charges in or on the support outside the metal particle is not reproduced.

It should be noted that the experimental particle shape shown in Figure 2 is broadened by the finite radius of the AFM tip which according to producer's specifications amounts to 25 nm. The effect was studied in detail,[24] and the final results [18] are reported for the deconvoluted particle shape, with the true particle radius given as R^* in place of R. The

deconvolution method is described in the Electronic Supplementary information of the companion paper.[18] The influence of the finite tip size on the Kelvin signal is discussed further below.

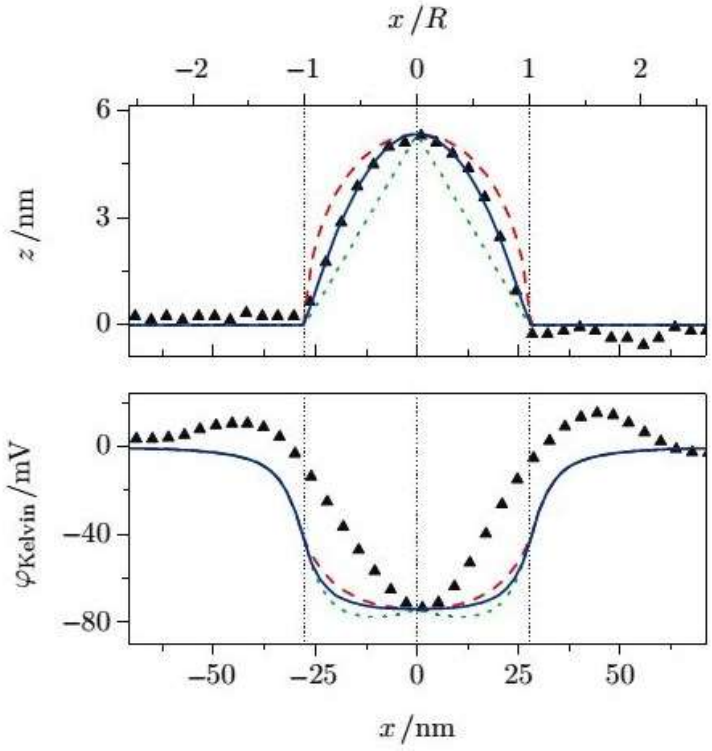

Figure 2. Upper entry: Comparison of an experimental particle profile (Pt/TiO_2, black triangles) with the ellipsoidal (dashed red line), conical (dotted green line) and parabolic (continuous blue line) simulation models. Note that the particle is 55 nm wide but only 5.3 nm high. Lower entry: Best simulation based on Sasahara's model that represents the interface as a conventional capacitor that has two parallel plates with homogeneously and symmetrically distributed charges.

Modification of the model after Hägglund and Zhdanov [8]

It can be argued that the above model of a one dimensional Schottky contact is only valid for macroscopic flat junctions between metal and semiconductor with a thickness that exceeds the thickness of the depletion layer (typically >100 nm).[8] The conventional treatment of

Schottky contacts [25] is thus not valid for nanoparticles which are often considerably thinner. Hägglund and Zhdanov therefore proposed a model based on the method of image charges for a disc-shaped (*i.e.* cylindrical) metal nanoparticle on a planar semiconductor support, and they introduced the real relative electrical permittivity of the support, e_S, (with a value of 110 for TiO_2) and of the metal particle, $e_M = 1$.[8] Charges located in the metal at its interface to the support (Q_M) on the outer particle surface (Q_{OS}) and corresponding charges in the support (Q_S) are distributed in hemispheres with a radius depending on the concentration of electron accepting or donating species. Alternatively, the charges on the support are assumed to reside in a homogeneous planar layer. The number of charges is determined to fulfill the central condition of a constant electrostatic potential inside the metal particle, which is accurate as long as the particle is homogeneous. These models are displayed in Figure 3 for both possible polarities, *i.e.* a *p*-type semiconductor where excess charges are transferred from the metal to the semiconductor, and an *n*-type semiconductor where the charge transfer is from the semiconductor to the metal. That charges are homogeneously distributed and confined strictly within a certain radius are bold constraints, but models which describe more realistic distributions require too many fit parameters and do not lead to more meaningful answers.

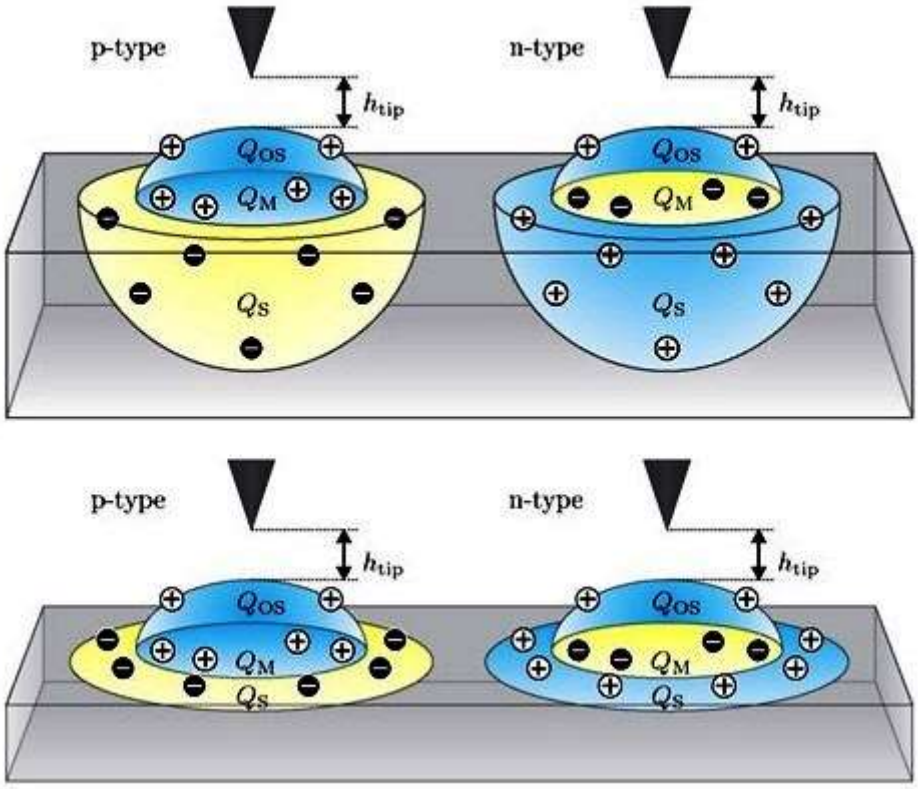

Figure 3. Charge distribution with two hemi-spherical charge distributions (top) and one hemi-spherical distribution for the metal and a planar, circular distribution for the support (bottom). Positive charges balance negative charges ($Q_{OS} + Q_M + Q_S = 0$). *p*-type: Positive charges (Q_{OS}) located at the outer particle surface and Q_M at the particle-support interface; negative charges (Q_S) located inside the support. *n*-type: Positive charges (Q_{OS}) located at particle surface and Q_S inside the support, negative charges (Q_M) located at the particle-support interface. The radius of the particle at the support interface is denoted by *R* (or later *R** after correction for broadening due to the AFM tip radius), and the radius of the charge distribution in the support is $R_S \geq R$. R_S is determined from the simulation of the Kelvin signal, while *R* is fixed as measured in the experiment.

Our intention is to approve or discard an assumed distribution model with the help of the experimental signal shape. It is therefore necessary to calculate the signal intensity not only at a single point above the center of the particle but along the scanning coordinate.

By using the method of image charges the potential inside and above the particle with $z \geq 0$ can be calculated as the sum of the different contributions

$$\varphi(x,z) = \sum_{\mathrm{i}} \varphi_{\mathrm{i}} \tag{6}$$

The potential φ_{OS} originating in the charges Q_{OS} at the outer particle surface and their mirror charges is given by

$$\varphi_{\mathrm{OS}}(x,z) = \frac{1}{4\pi\varepsilon_0} \cdot \frac{Q_{\mathrm{OS}}}{A_{\mathrm{OS}}} \cdot \frac{1}{e_M} \left(\int_{\phi=0}^{2\pi} \int_{\vartheta=0}^{\frac{\pi}{2}} \frac{1}{|\overrightarrow{pr}|} \mathrm{d}A - \frac{e_{\mathrm{M}} - e_{\mathrm{S}}}{e_{\mathrm{M}} + e_{\mathrm{S}}} \int_{\vartheta=0}^{2\pi} \int_{\varphi=\frac{\pi}{2}}^{\pi} \frac{1}{|\overrightarrow{pr}|} \mathrm{d}A \right) \tag{7}$$

where distances $|\overrightarrow{pr}|$ and surface elements dA are expressed in the respective coordinate systems depending on the particle shapes and listed in Table 1. In polar coordinates, the potential φ_{M} due to the charges Q_{M} located in the metal near the particle support interface and their mirror charges is

$$\varphi_{\mathrm{M}}(x,z) = \frac{1}{4\pi\varepsilon_0} \cdot \frac{Q_{\mathrm{M}}}{\pi R^2} \cdot \frac{1}{e_M} \left(1 + \frac{e_{\mathrm{M}} - e_{\mathrm{S}}}{e_{\mathrm{M}} + e_{\mathrm{S}}} \right) \int_{r=0}^{R} \int_{\phi=0}^{2\pi} \frac{1}{\sqrt{x^2 + r^2 - 2xr\cos\phi + z^2}} \mathrm{d}\phi \, \mathrm{d}r \tag{8}$$

and the potential due to the charges Q_{S} located in the support inside a hemisphere with radius R_{S} results in spherical polar coordinates to

$$\varphi_{\mathrm{S}}(x,z) = \frac{1}{4\pi\varepsilon_0} \cdot \frac{3Q_{\mathrm{S}}}{2\pi {R_{\mathrm{S}}}^3} \cdot \frac{2}{e_{\mathrm{M}} + e_{\mathrm{S}}} \int_{r=0}^{R_{\mathrm{d}}} \int_{\phi=0}^{2\pi} \int_{\vartheta=0}^{\frac{\pi}{2}} \frac{r^2 \sin\varphi}{\sqrt{x^2 + r^2 - 2\mathrm{r}(z\cos\vartheta + x\sin\vartheta\cos\phi) + z^2}} \, \mathrm{d}\vartheta \, \mathrm{d}\phi \, \mathrm{d}r \tag{9}$$

For a circular charge distribution near the interface inside the support the potential results to

$$\varphi_{\mathrm{S}}^{*}(x,z) = \frac{1}{4\pi\varepsilon_0} \cdot \frac{Q_{\mathrm{S}}}{\pi {R_{\mathrm{S}}}^2} \cdot \frac{2}{e_{\mathrm{M}} + e_{\mathrm{S}}} \int_{r=0}^{R_{\mathrm{d}}} \int_{\phi=0}^{2\pi} \int_{\vartheta=0}^{\frac{\pi}{2}} \frac{r^2 \sin\varphi}{\sqrt{x^2 + r^2 - 2rx\cos\phi + (z+d)^2}} \, \mathrm{d}\vartheta \, \mathrm{d}\phi \, \mathrm{d}r \tag{10}$$

Integrals in equations (7)-(10) have to be solved numerically.

For the special case of $x = 0$, the following analytical solutions for integrals (8)-(10) can be found:

$$\varphi_{\mathrm{M}}(0,z) = \frac{1}{4\pi\varepsilon_0} \frac{2Q_{\mathrm{M}}}{R^2} \left(\frac{1}{e_{\mathrm{M}}} + \frac{e_{\mathrm{M}} - e_{\mathrm{S}}}{e_{\mathrm{M}} + e_{\mathrm{S}}} \right) \left(\sqrt{R^2 + z^2} - \sqrt{z^2} \right) \tag{11}$$

$$\varphi_{\mathrm{S}}(0,z) = \frac{1}{4\pi\varepsilon_0} \cdot \frac{Q_{\mathrm{S}}}{{R_{\mathrm{S}}}^3} \cdot \frac{2}{e_{\mathrm{M}} + e_{\mathrm{S}}} \left(\left(\sqrt{{R_{\mathrm{S}}}^2 + z^2} - z \right)^2 + \frac{2R_{\mathrm{S}}}{z} \left(R_{\mathrm{S}} + z - \sqrt{{R_{\mathrm{S}}}^2 + z^2} \right) \right) \tag{12}$$

$$\varphi_{\mathrm{S}}^{*}(0,z) = \frac{1}{4\pi\varepsilon_0} \cdot \frac{2Q_{\mathrm{S}}}{{R_{\mathrm{S}}}^2} \cdot \frac{2}{e_{\mathrm{M}}+e_{\mathrm{S}}} \left(\sqrt{{R_S}^2 + z^2} - z - d \right) \tag{13}$$

This analytical solution can be used in most cases, and it simplifies the analysis considerably. Charge neutrality is given by

$$Q_{\mathrm{OS}} + Q_{\mathrm{M}} + Q_{\mathrm{S}} = 0 \tag{14}$$

Table 1: Surface elements dA and tip charge distances $|\overrightarrow{pr}|$ expressed in the respective coordinates $\vec{r}$ with the radial distance r, azimuthal angle ϑ and polar angle φ, radius R of the particle at the interface and its height H, and the tip position $\vec{p} = (x, 0, z)$. The origin of the coordinate system is at the center of the interface, $\vec{p} = (0,0,0)$.

particle shape	$\vec{r}$	$\frac{1}{\lvert\overrightarrow{pr}\rvert}\mathrm{d}A$
ellipsoid	$r\begin{pmatrix}\sin\varphi\cos\vartheta\\ \sin\varphi\sin\vartheta\\ \frac{H}{R}\cos\varphi\end{pmatrix}$	$\frac{R\sin\vartheta\sqrt{H^2\sin^2\vartheta + R^2\cos^2\vartheta}}{\sqrt{x^2 - 2xR\sin\vartheta\cos\phi + R^2\sin^2\vartheta + (z - H\cos\vartheta)^2}}\ \mathrm{d}\vartheta\,\mathrm{d}\phi$
cone	$r\begin{pmatrix}\sin\varphi\cos\vartheta\\ \sin\varphi\sin\vartheta\\ \frac{H}{R} - \frac{H}{R}\sin\varphi\end{pmatrix}$	$\frac{R\sin\vartheta\sqrt{H^2 + R^2}}{\sqrt{x^2 - 2xR\sin\vartheta\cos\phi + R^2\sin^2\vartheta + (z + H\sin\vartheta - H)^2}}\ \mathrm{d}\vartheta\,\mathrm{d}\phi$
paraboloid	$r\begin{pmatrix}\sin\varphi\cos\vartheta\\ \sin\varphi\sin\vartheta\\ \frac{H}{R}\cos^2\varphi\end{pmatrix}$	$\frac{R\sin\vartheta\sqrt{4H^2\sin^2\vartheta + R^2}}{\sqrt{x^2 - 2xR\sin\vartheta\cos\phi + R^2\sin^2\vartheta + (z - H\cos^2\vartheta)^2}}\ \mathrm{d}\vartheta\,\mathrm{d}\phi$

Determination of parameters by solving the system of equations

Equations (7) – (14) are a set of non-linear equations with the four free variables Q_{OS}, Q_{M}, Q_{T} and R_{S}. The experimental Kelvin signal and the assumption of a constant potential $\varphi_{const.}$ inside the metal particle allow us to solve this set of equations.

The experimental Kelvin signal is the negative to the potential φ_{tip}

$$\varphi(0, z_{tip}) = \varphi_{\mathrm{tip}} = -\varphi_{\mathrm{Kelvin}} \tag{15}$$

And the vertical tip position z_{tip} is calculated as the sum of the actual particle height H at a given position and the scan height h_{tip}.

We chose positions at the top, the bottom and in the middle along the central axis to fulfill the condition of a constant potential and the constraint of charge neutrality (eqn. 14).

$$\varphi(0,0) = \varphi\left(0, \frac{H}{2}\right) = \varphi(0, H) = \varphi_{\mathrm{const}} \tag{16}$$

$Q_{\mathrm{OS}}, Q_{\mathrm{M}}, Q_{\mathrm{S}}, R_{\mathrm{S}}$ and φ_{const} are obtained by solving the non-linear equation system at the positions given by eqns. (15) and (16) numerically. Q_{OS} is at this point only a phenomenological fitting parameter without any assignment of a chemical identity in the semiconductor. Its interpretation is discussed in the companion paper.[18]

Simulation of Kelvin signals

Equations (6)-(10) and the parameters $Q_{\mathrm{OS}}, Q_{\mathrm{M}}, Q_{\mathrm{S}}$ and R_{S} determined at $\mathrm{x} = 0$ allow us to calculate the Kelvin signal in dependence of the lateral tip position $\mathrm{x}_{\mathrm{tip}}$ and the vertical tip position z_{tip} above the model particle. This simulated potential profile is then compared with the measured Kelvin profile, with

$$\varphi\left(\mathrm{x}_{\mathrm{tip}}, z_{\mathrm{tip}}\right) = -\varphi_{\mathrm{Kelvin}} \tag{17}$$

The solutions of the simulations based on the various models are displayed in Figure 4. The top row gives the topographic compared with the assumed shape profiles. More important are the second and the third row which give the results for the hemispherical and the planar charge distribution in the support – for the *p*-type case on the left and the *n*-type case on the right. Qualitatively, both directions of charge transfer can be reproduced, but it is obvious that the *n*-type semiconductor solutions match the experiment better. The charge distributions of the *p*-type are too broad and do not reproduce the rim in the experimental signal, in contrast to the *n*-type model, although the agreement is not fully quantitative.

In all cases the constant potential in the metal nanoparticle is in the range +80 mV < φ_{const} < 142 mV, dictated to be positive by the experimentally clearly negative Kelvin potential. This is probably the parameter which is most relevant for the catalytic properties. For the model which shows the best agreement with experiment, the *n*-type model with parabolic particle shape and a planar charge distribution in the semiconductor φ_{const} amounts to 111 mV, and the charge densities are +0.37 *e* per nm^2 for ρ_S, –0.32 *e* nm^{-2} for ρ_M, and 0.00057 *e* nm^{-2} for ρ_{OS}, while R_S is only 0.92 *R*, *i.e.* the charge zone does not quite reach the full, uncorrected radius of the particle, but it exceeds the true particle radius *R** (see companion paper).[18] The charge density on the outer surface of the metal particle, ρ_{OS}, is clearly much smaller than the others, and it can be neglected at no significant loss.

The interesting fact that the opposite polarity with a *p*-type support can provide qualitatively similar curves is explained by charge densities of –3.1 *e* nm^{-2} for ρ_S, +3.1 *e* nm^{-2} for ρ_M, *i.e.* an order of magnitude larger than for the *n*-type, but with opposite sign, nevertheless φ_{const} = 94 mV, and 0.00024 *e* nm^{-2} for ρ_{OS}, with $R_S \approx R$ (curve a). A much more detailed analysis than can be presented here is available online.[24] It reveals that a planar charge distribution ρ_S in the support cancels much of the counter charge ρ_M at the opposite interface in the metal, since the distance *d* = 0.2 nm between the two planes of opposite charge is small compared with the height of the tip, h_{tip} = 5.0 nm above the particle of 5.3 nm height. Thus, much of the observed Kelvin signal is due to the very small charge density ρ_{OS} at the metal-air interface and by the charge on the rim ($R_S \approx R$). Even if it makes a relatively small contribution to the total signal, reproduction of the signal shape around the rim is considered important for the distinction between the models. If ρ_S is forced to be zero (curve c) this causes R_S to be orders of magnitude larger than *R*. Further analysis shows that only the curves (a) represents a global minimum, (b) and (c) correspond to side minima. The different particle shapes do not significantly influence the results.

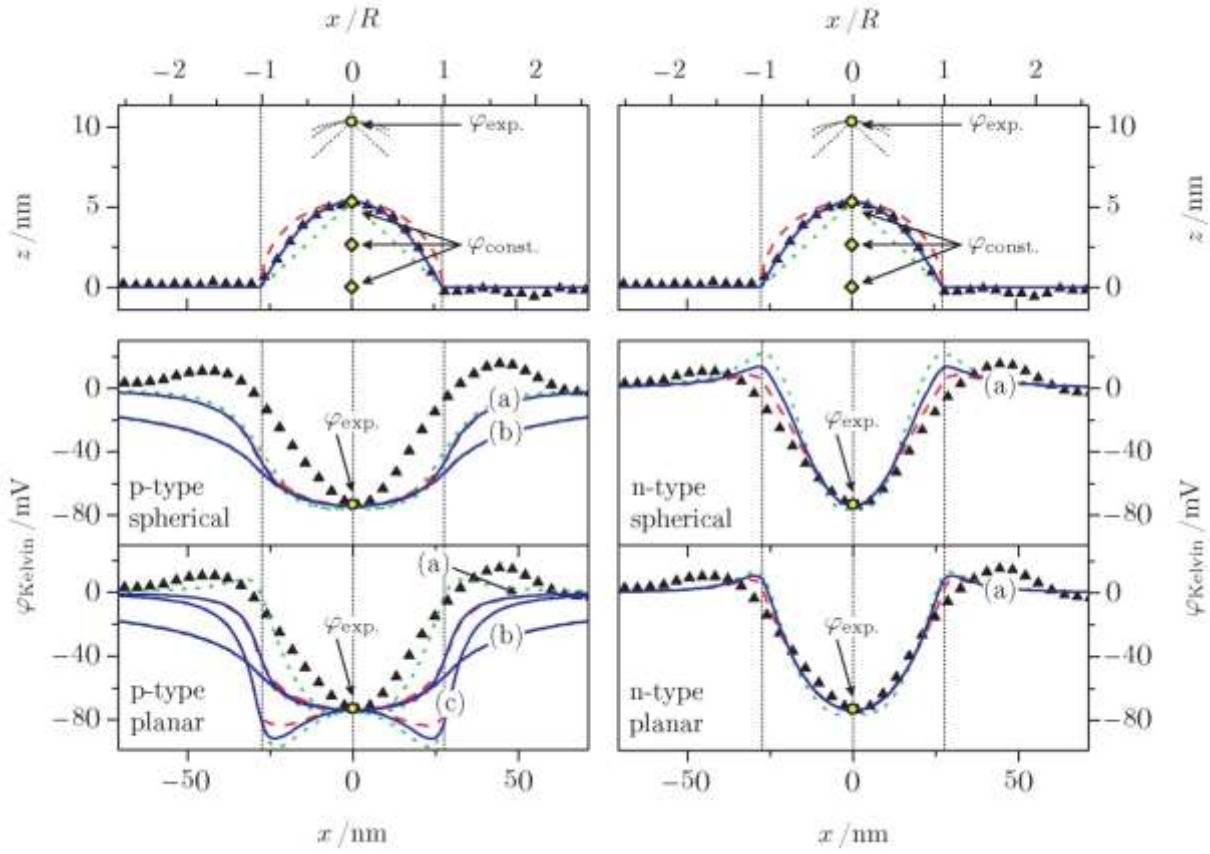

Figure 4. Simulated profiles using the experimental value $\varphi_{exp.}(0,z_{tip})$ and the condition that the potential inside the metal particle $\phi_{konst}(0, z)$ is the same at the positions z = 0, ½H und H (yellow symbols) for the ellipsoidal (red dashed), parabolic (full blue line) and cone-shaped (green, dotted) particle shape, and experimental points (black triangles). The left side shows the solutions with charge transfer from the particle to the n-type support, the right hand side the opposite polarization, each with a hemispherical and a planar charge zone. The curves are for $R_S \approx R$ (a), $R_S \gg R$ (b) and for $Q_S = 0e$ (c).

While the simulated curves of the *n*-type semiconductor (right hand side of Figure 4) match the experimental results better than those of the *p*-type, further analysis shows that the constant potential inside the metal particle is much better obeyed for the particle on the *p*-type

than on the *n*-type semiconductor. These conflicting findings do therefore not permit a reliable discrimination between the *n*-type and the *p*-type model at this point.

Intending to improve the fits, two further rounds in the analysis were undertaken in which one and two additional experimental points off-center of the particle at $x = ½R_S$ and $1R_S$ were employed. The results are displayed in Figure 5. In contrast to Figure 4 which uses only the center point we now obtain for the planar charge distribution a slightly better match including a small inverted rim for the *p*-type support while the simulated trace for the n-type support has lost its inverted rim. As before, the spherical charge distribution does not lead to a satisfactory match.

φ_{const} amounts to 106 mV, and the charge densities are –0.13 *e* nm^{-2} for ρ_S, +0.17 *e* nm^{-2} for ρ_M, and 0.00047 *e* per nm^2 for ρ_{OS}, while R_S is 1.2 *R* for the *p*-type support with planar charge zones. All *n*-type simulations yield R_S in the range 0.3-0.4 *R* and 0.4-0.5 *R* for the hemispherical and for the planar charge distributions, respectively. These values are very low and difficult to justify for a Schottky contact. The charge density on the metal particle outer surface remains very small in all cases. Remarkably, the charge densities at the interface are more than an order of magnitude smaller than in the fits presented in Figure 4, indicating that this is an important parameter which is determined more reliably when additional experimental points are used. ρ_S was therefore investigated systematically in more detail and used as a fixed parameter which was varied in a wide range ($10^{-9} \le \rho_S \le 10$ e nm^{-2} for the *n*-type support). For the *p*-type support, no solutions were found for $|\rho_S| < 0.02$ e nm^{-3} (hemispherical) or $|\rho_S| < 0.1$ e nm^{-2} (planar), which is equivalent to $R_S > 0.5$ *R*. A fixed value of the homogeneous charge distribution ρ_S is equivalent to a fixed value of R_S since the two parameters are related via the charge in the support $Q_S = Q_M + Q_{OS}$. Specifically, $Q_S = \rho_S \pi R_S^2$ for the planar and $Q_S = 2\rho_S \pi R_S^3/3$ for the hemispherical charge distribution. For the

determination of the parameters it is thus sufficient to use the experimental potential $\varphi_{exp}(0,z_{tip})$ and a constant potential $\varphi_{const}(0,z)$ for $z = 0$ and $z = H$.

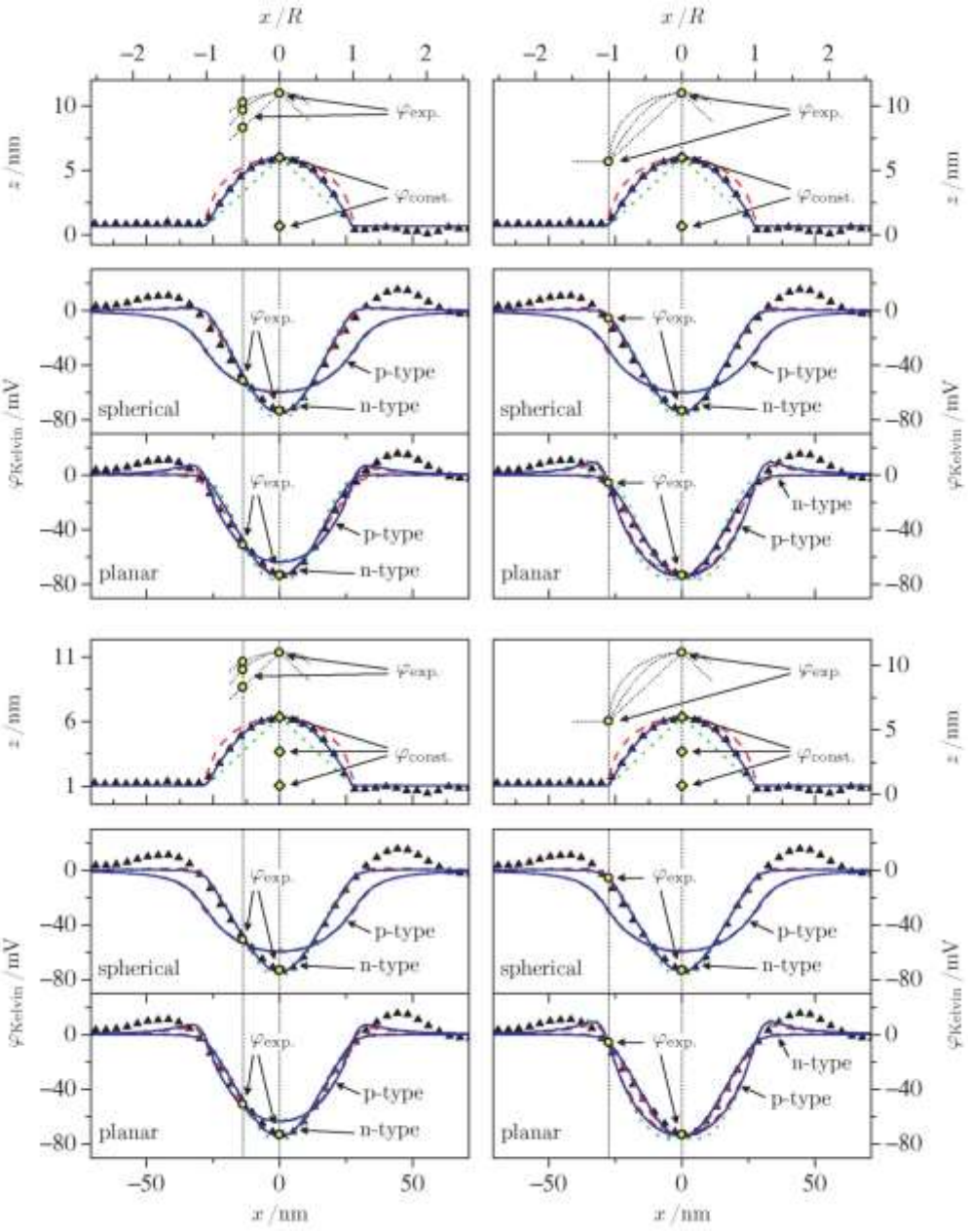

Figure 5. Kelvin signals resulting from simulations with one additional experimental point $\varphi_{exp}(x,z_{tip})$ at $x = R/2$ (left column) or $x = R$ (right column). It replaces the point at constant potential $\varphi_{const}(0,z)$ at $z = H/2$ (upper row), or it is used as additional, fifth point for the determination of the simulation parameters (lower row). See Figure 4 for the meaning of the symbols.

The results of the analysis are plotted and discussed in the supplementary information as a function R_S/R and of Q_S (Figures S1 and S2) and in detail also in ref. 24. In short the findings are as follows:

- In function of R_S/R, all parameters show a discontinuity with asymptotic behavior at $R_S/R = 0.72$ for the hemispherical and $R_S/R = 0.99$ for the planar charge distributions. At this point, the charges Q_S and Q_M change sign, which is equivalent to a transition between *n*-type and *p*-type support. It is plausible that R_S is smaller for the hemispherical distribution since a given charge Q_M that is to be compensated at a given charge density requires a larger radius when accommodated in a single layer.
- Q_S and Q_M are nearly identical in magnitude but of opposite sign. Their sum is compensated by the charge on the outer metal surface, Q_{OS}, which is three orders of magnitude smaller than $|Q_S|$ and $|Q_M|$. Interestingly, Q_{OS} shows the same behavior as φ_{const}, the potential in the metal particle. This demonstrates that φ_{const} which is probably the catalytically relevant property has its origin in a relatively small number of deficit electrons on the outer particle surface, Q_{OS}, while the much larger number of charges which are located at the two sides of the interface cancel each other to a large extent. Q_{OS} is positive over a very wide range of ρ_S, independent of the *p*-type or *n*-type nature of the support. This has its origin in the fact that $\varphi_{exp}(0,z_{tip})$ is a fraction of $\varphi_{const}(0,H) = \varphi_{const}(0,0)$, with the same sign.
- The asymptotic behavior near the discontinuities in Figures S1 and S2 represent high charge densities which are not physically meaningful since this situation corresponds to high Coulomb repulsion energies.

Simulated curves for the *n*-type support are shown for three selected prefixed values of charge densities ρ_S in Figure 6. All curves except the one for $\rho_S = +0.12\ e\ nm^{-2}$ for the planar charge zone exhibit a clear change of sign with positive values of the Kelvin signal, but the

maximum is located at $R_S \approx R$, which is not compatible with experiment. It is obvious that the high charge densities although still remote of the unphysical discontinuities do also not match the experimental behavior.

A similar set of curves is shown in Figure 7 for the *p*-type support. The high charge densities now display a double peak structure, which was never observed in the experiment. The low charge densities lead to too broad curves, but remarkably, an intermediate charge density $\rho_S = -0.020\ e\ \mathrm{nm}^{-2}$ for the planar charge zone provides a highly satisfactory agreement with experiment (highlighted in red frame). In particular, it reproduces also the inverted zone very well.

Additional fit parameters can in principle improve the agreement between experiment and simulation further when additional experimental points are used. With this aim, the charge zone on the outer particle surface was partitioned into three zones near the support surface, on top of the particle, and one intermediate zone. While in principle the strategy works, it is difficult to obtain significant new insight due to the increased complexity. We will therefore skip these results. More details can be found in ref. 24.

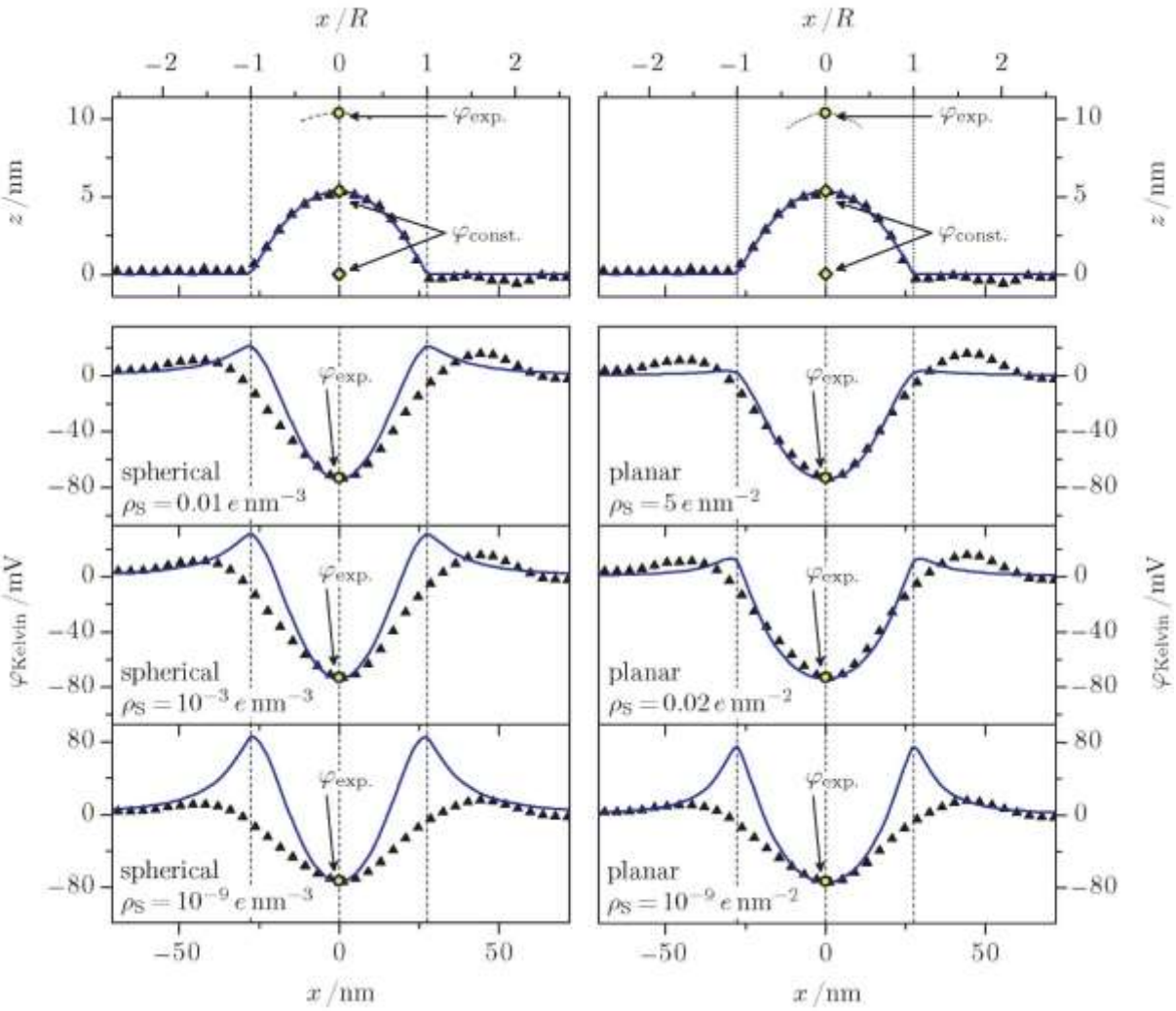

Figure 6. Simulated Kelvin signal for transfer of a fixed negative charge density ρ_S from a parabolic metal particle to the *n*-type support with a spherical (left) and a planar (right) charge distribution. Further experimental values used were $\varphi_{exp}(0,z_{tip})$, $\varphi_{const}(0,0)$ and $\varphi_{const}(0,H)$. For the meaning of the symbols see the caption of Figure 4.

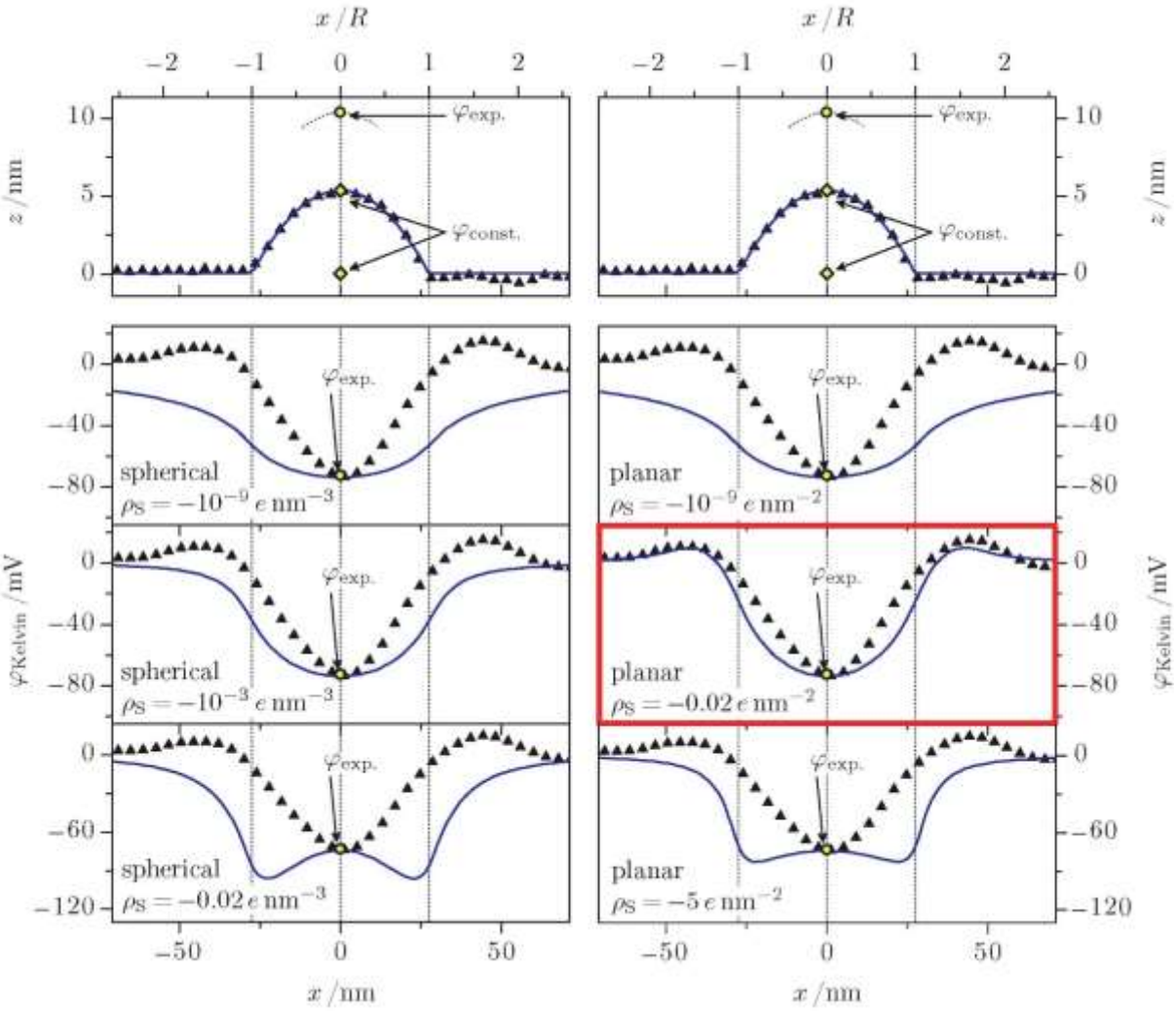

Figure 7. Simulated Kelvin signal for transfer of a fixed negative charge density ρ_S from a parabolic metal particle to a *p*-type support with a spherical (left) and a planar (right) charge distribution. Further experimental values used were $\varphi_{exp}(0,z_{tip})$, $\varphi_{const}(0,0)$ and $\varphi_{const}(0,H)$. The overall best match of a simulated curve with the experimental Kelvin trace is framed in red. For the meaning of the symbols see the caption of Figure 4.

One may also imagine other variations of the charge distribution model. At present, homogeneous charge densities were assumed in the support, but ρ_S may actually be different underneath the particle and for radii > *R*. However, for the best match of the model particle, equal charges Q_M and Q_S were found. Equal charge *densities* would thus not leave any room

to accommodate any charges in the trough on the rim around the particle, which would not be consistent with experiment.

The charge density $\rho_S = -0.020\ e\ \mathrm{nm}^{-2}$ for the planar charge zone in the TiO_2 support is a material property which depends not only on the elemental composition but also on the pretreatment conditions in a given atmosphere. For metal clusters of different size supported on the same material in the identical sample it is expected to be the same. The value of ρ_S determined here was therefore fixed for the complete analysis of the samples Pt/TiO_2. The strategy of first determining ρ_S to be fixed for the subsequent analysis was also followed for the other supports. These values are given in Table 1 of the experimental companion paper.[18]

Possible effects of the finite tip size on the Kelvin probe signal

The topography data have been deconvoluted for the finite size of the AFM tip as described in the Electronic Supplementary Information of the companion paper.[18] Most Pt particles on all three supports are well defined and have a true diameter of 50-100 nm (Figure 7). According to the curve for parabolic particle shapes the correction amounts to ca. 35% for the diameters of the smallest particles, and less for the larger ones (Figure S4b of the companion paper).[18] The particles are quite flat with a relatively steep slope near the rim and few of them exceeding 12 nm in height. The larger particles are also higher. Rh and Pd particles formed agglomerates with complicated profiles for which the analysis is naturally less accurate.

Since the Kelvin probe data were recorded with a tip that was retracted by 5-7 nm it was assumed that the tip is a point-like probe of the potential. While this led to good agreement between experiment and simulation and also to agreement with up to date literature about the direction of charge transfer [26] concerns have been raised about the validity of the approximation assuming a point-like tip and fixed electrical charges, in particular in the

presence of conductive samples,[27-30] and it was suggested to involve also van der Waals forces.[31] Most charges in the oxide support are fixed to defects, and in the metal nanoparticle the charges at the interface are largely immobilized by the attraction to the counter charge in close proximity across the interface, but there are mobile conduction electrons which render the particles polarizable by the applied voltage on the tip. This affects not only the derived charge concentration and distribution, it also questions the assumption of a constant electrostatic potential inside the metal. A further effect may be the result of the interaction of the sample with the finite size tip, in particular when it is located above the rim of the particle. This situation which is illustrated in Figure S3 of the ESI enhances the Kelvin singal. It may be the origin of the more plateau-like shape at the top of the signal compared with the rounded shape of the topography seen in particular in Figure 2 of the companion paper.[18]

Taking all these effects into account would render the already complex simulations much more involved. It would certainly affect the values of the derived numbers for charge distributions but not their order of magnitude and certainly not the main conclusion that the direction of electron transfer is from the metal to the oxide and of the positive electrostatic potential of the metal due to charge polarization.

CONCLUSIONS

An extension of the model of Hägglund and Zhdanov [8] for the description of a Schottky contact permits a near-quantitative fit of the experimental Kelvin probe signal of a nanometer size Pt particle on a TiO_2 metal oxide support. The Kelvin signal which is negative relative to the support can to a first approximation be explained on the basis of both an *n*-type support with positive charge density near the interface, compensated approximately by negative charge density in the metal near the interface, and on the basis of a *p*-type support with opposite charge polarity. In both cases there is a net transfer of electrons from the Pt particle to the support, leaving a small positive charge density on the outer surface of the metal

particle. It is this positive charge density that determines the constant electronic potential φ_{const} within the metal which is likely responsible for the metal-support interaction. Comparison of the simulated curves of the Kelvin potential with the experimental trace allows to exclude a hemispherical charge distribution in the support and suggests that most of the charge densities are located in planar layers on the two sides of the interface.

For the analyzed Pt model particle of 55 nm diameter and 5.3 nm height on TiO_2, clearly the best agreement is found for the case of a *p*-type support with a negative charge density, ρ_S = –0.020 *e* nm^{-2}, with φ_{const} = 106 mV which leads to the experimentally measured potential $\varphi(x_{tip}, z_{tip}) = -\varphi_{Kelvin}$ = 73 mV at the retracted tip position 5 nm above the highest point of the Pt particle. As expected, the sign of the experimentally measured Kelvin potential permits a direct conclusion about the sign of the electrical potential in the particle. The charge density in the metal across the interface is ρ_M = +0.057 *e* nm^{-2}, while the charge density on the outer metal surface (the metal/air interface), is $\rho_{OS} = 4.6\times10^{-4}$ *e* nm^{-2}, two orders of magnitude less than the charge densities at the interface. The circular, planar charge zone in/on the support extends by a factor 1.7 beyond the uncorrected physical diameter of the Pt particle. Experimentally, this zone around the particle is observed as a characteristic rim around the particle in the Kelvin potential measurements.

Supporting Information. Further details of the results of fits to the Kelvin signal are available in supporting information. This material is available free of charge via the Internet at http://pubs.acs.org.

AUTHOR INFORMATION

* Corresponding author: e.roduner@ipc.uni-stuttgart.de, Phone: +27 12 420 4474

† Present address: Ontorix GmbH, Boschstraße 10, D-73734 Esslingen am Neckar, Germany

Author Contributions:

The manuscript was written through contributions of all authors. All authors have given approval to the final version of the manuscript. TK has conducted the experiment and designed and performed the analysis. ER has conceived and supervised the work.

ACKNOWLEDGMENTS

The work was performed within the Collaborative Research Center SFB 706 (Selective catalytic oxidations using molecular oxygen) in Stuttgart and funded by the German Research Foundation (DFG).

REFERENCES

1) Acerbi, N.; Tsang, S. C.; Golunski, S.; Collier, P. A Practical Demonstration of Electronic Promotion in the Reduction of Ceria-Coated PGM Catalysts. *Chem. Commun.* **2008**, 1578-1580.
2) Frost, J. C. Junction Effect Interaction in Methanol Synthesis. *Nature*, **1988**, *334*, 577-580.
3) Solymosi, F.; Importance of the Electric Properties in the Carrier Effect. *Catal. Rev.*, **1968**, *1*, 233-255.
4) Ioannides, T.; Verykios, X. E. Charge Transfer in Metal Catalysts Supported on Doped TiO_2: A Theoretical Approach Based on Metal-Semiconductor Contact Theory. *J. Catal.* **1996**, *161*, 560-569.
5) Ioannides, T. Comment on: "Nm-Size Metal Particles on a Semiconductor Surface, Schottky Model etc." *Surf. Sci.* **2003**, *530*, 216-218.
6) Zhdanov, V. P. Nm-Size Metal Particles on a Semiconductor Surface, Schottky Model etc. *Surf. Sci.* **2002**, *512*, L331-L334.

7) Zhdanov, V. P. Reply to Comment on "Nm-Size Metal Particles on a Semiconductor Surface, Schottky Model etc." *Surf. Sci.* **2003**, *530*, 219-220.

8) Hägglund, C.; Zhdanov, V. P. Charge Distribution on and near Schottky Nanocontacts. *Physica E-Low-Dim. Syst. Nanostruc.* **2006**, *33*, 296-302.

9) Akubuiro, E. C.; Verykios, X. E. Effects of Dopants on Performance of Metal Crystallites: 2. Further Characterization of Doped Supports and Catalysts. *J. Catal.*, **1988**, *113*, 106-119.

10) Koussathana, M.; Vamvouka, N.; Tsapatsis, M.; Verykios, X. E. Hydrogenation of Aromatic Compounds over Noble Metals Dispersed on Doped Titania Carriers. *Appl. Catal.*, **1992**, *80*, 99-113.

11) Koussathana, M.; Vamvouka, N.; Verykios, X. E., Naphthalene Hydrogenation Reactivity of Rhodium-Rhenium and Ruthenium-Rhenium Formulations Dispersed on Doped Titania. *Appl. Catal.*, **1993**, *95*, 211-220.

12) Akubuiro, E. C.; Verykios, X. E., Effects of Altervalent Cation Doping on Electrical Conductivity of Platinized Titania. *J. Phys. Chem. Solids*, **1989**, *50*, 17-26.

13) Howe, R. F.; Grätzel, M. EPR Observation of Trapped Electrons in Colloidal Titanium Dioxide. *J. Phys. Chem.* **1985**, *89*, 4495-4499.

14) Erdal, S.; Kongshaug, C.; Bjørheim, T. S. ; Jalarvo, N.; Haugsrud, R.; Norby, T. Hydration of Rutile TiO_2: Thermodynamics and Effects on *n*- and *p*-Type Electronic Conduction. *J. Phys. Chem.* C, **2010**, *114*, 9139-9145.

15) Warren, D. S.; Shapira,Y.; Kisch, H.; McQuillan, A. J. Apparent Semiconductor Type Reversal in Anatase TiO_2 Nanocrystalline Films. *J. Chem. Phys. C*, **2007**, *111*, 14286-14289.

16) Roduner, E. *Nanoscopic Materials: Size-Dependent Phenomena and Growth Principles*. Royal Society of Chemistry, Cambridge, 2014.

17) Jacob, M.; Levanon, H.; Kamat, P. V.; Charge Distribution between UV-Irradiated TiO_2 and Gold Nanoparticles: Determination of Shift in the Fermi Level. *Nano Lett.*, **2003**, *3*, 353-358.

18) Kittel, T.; Roduner, E.; Charge Polarization at Catalytic Metal-Support Junctions. Part A: Kelvin Probe Force Microscopy Results of Noble Metal Nanoparticles. *J. Phys. Chem. C* (companion paper).

19) Walrath, J. C.; Lin, Y.-H.; Goldman, R. S. Profiling the Local Carrier Concentration Across a Semiconductor Quantum Dot. *Appl. Phys. Lett.*, **2015**, *106*, 192101.

20) Melitz, W.; Shen, J.; Kummel, A. C.; Lee, S. Kelvin Probe Force Microscopy and its Application, *Surf. Sci. Rep.* **2011**, *66*, 1-27.

21) Sasahara, A.; Hiehata, K.; Onishi, H. Charge Transfer Observed by a Kelvin Probe Microscope. *Catal. Surveys Asia* **2009**, *13*, 9-15.

22) Hiehata, K.; Sasahara, A.; Onishi, H. Local Work Function Analysis of Pt/TiO_2 Photocatalysts by a Kelvin Probe Force Microscope. *Nanotech.* **2007**, *18*, 084007.

23) Sasahara, A.; Pang, C. L.; Onishi, H. Local Work Function of Pt Clusters Vacuum-Deposited on a TiO_2 Surface. *J. Phys. Chem. B* **2006**, *110*, 17584-17588.

24) T. Kittel, *Untersuchung von Edelmetallpartikeln auf Metalloxidträgern mittels Kelvinsonden-Rasterkraftmikroskopie*. PhD Thesis, University of Stuttgart, 2015. http://elib.uni-stuttgart.de/opus/volltexte/2015/9871/

25) Ludeke, R. in: Horn, K. and Scheffler, M. (Eds.), *Electronic Structure; Handbook of Surface Science*, vol. 2, Elsevier, Amsterdam, **2000**, p. 749 ff.

26) Lykhach, Y.; Kozlov, S. M.; Skála, T.; Tovt, A.; Stetsovich, V.; Tsud, N.; Dvořák, F.; Johánek, V.; Neitzel, A.; Mysliveček, J.; Fabris, S.; Matolin, V.; Neyman, K. M.; Libuda, J. Counting Electrons on Supporting Nanoparticles. *Nature Mat.* **2015**, *15*, 284-288.

27) Sacha, G. M.; Cardellach, M.; Segura, J. J.; Moser, J.; Bachtold, A.; Fraxedas, J.; Verdaguer, A. Influence of the Macroscopic Shape of the Tip on the Contrast in scanning Polarization Force Microscopy Images. *Nanotech.*, **2009**, *20*, 285704.

28) Sacha, G. M.; Gómez-Navarro, C.; Sáenz, J. J.; Gómez-Herrero, J. Quantitative Theory for the Imaging of Conducting Objects in Electrostatic Force Microscopy. *Appl. Phys. Lett.* **2006**, *89*, 173122.

29) Sacha, G. M.; Shagún, E.; Sáenz, J. J. A method for Calculating Capacitances and Electrostatic Forces in Atomic Force Microscopy. *J. Appl. Phys.* **2007**, *101*, 024310.

30) Olsson, L.; Lin, N.; Yakimov, V.; Erlandsson, R. A Method for in-situ Characterization of Tip Shape in AC-Mode Atomic Force Microscopy Using Electrostatic Interaction. *J. Appl. Phys.* **1998**, *84*, 4060-4064.

31) Saint Jean, M.; Hudlet, S.; Guthmann, C.; Berger, J. Van der Waals and Capacitive Forces in Atomic Force Microscopies. *J. Appl. Phys.* **1999**, *86*, 5245-5248.

Graphical abstract